ECS | The Electrochemical Society
Advancing solid state & electrochemical science & technology

A System Identification Approach to Estimate Lithium-Ion Battery Entropy Coefficients

View the article online for updates and enhancements.

You may also like

A System Identification Approach to Estimate Lithium-Ion Battery Entropy Coefficients

W. D. Widanage,[1,a,z] O. Queisser,[2,b] S. Paarmann,[2,3,c] L. Cloos,[2] and T. Wetzel[2]

[1]WMG, University of Warwick, Coventry CV4 7AL, United Kingdom
[2]Institute of Thermal Process Engineering (TVT), Karlsruhe Institute of Technology (KIT), Kaiserstr. 12, 76131 Karlsruhe, Germany
[3]Department of Mechanical Engineering, Imperial College London, London SW7 2AZ, United Kingdom

Improving lithium-ion battery thermal simulations requires identification of all the relevant heat source terms. While Joule heating is always considered, reversible heat is important for mild to low C-rates, but is often ignored. Characterising reversible heat requires determining the cell's entropy coefficient as a function of the state-of-charge, which is experimentally time-consuming. In this paper, we take a dynamic view point between the cell open-circuit-voltage and cell temperature to arrive at the entropy coefficient. Called the kernel-based method, a system identification procedure in the frequency domain is developed to estimate the entropy coefficient at each state-of-charge (SoC). The methodology is validated against the potentiometric method, which is considered as the reference procedure. The entropy coefficient was estimated over 21 SoC points and compared against the potentiometric approach and showed very good agreement across the entire SoC interval with a 57% reduction in time. All the experimental data and the Matlab code for data processing and reproducing of the results is made available together with the paper.

Lithium-ion batteries are indispensable in today's decarbonisation strategies. From electrification of the transport sector, grid storage, and consumer electronics, they play a crucial role as high energy density and high efficiency energy storage devices. Considerable research effort is underway to characterize and model the physical behavior of lithium-ion batteries. Among these efforts, modelling and simulation play an important role in the design and control of the subsequent battery product.

Models such as the Doyle-Fuller-Newman (DFN),[1] which accounts for physical mechanisms, to Equivalent Circuit Models (ECM) that take a phenomenological approach are used to enable such design and control applications. However, for any practical usefulness, these models have to be thermally coupled, and not only simulate the voltage response accurately but also simulate the cell's thermal behavior. Such models then facilitate the opportunities for lithium-ion battery applications. Characterising the heat generation source terms then becomes important for model development.

The total heat flow (in W) of a lithium-ion battery can be broadly divided into two source terms known as irreversible heat ($\dot{Q}_{\mathrm{irr}}$) and reversible heat ($\dot{Q}_{\mathrm{rev}}$).

$$\dot{Q} = \dot{Q}_{\mathrm{irr}} + \dot{Q}_{\mathrm{rev}} \qquad [1]$$

The total heat flow $\dot{Q}$ then appears as a source term in either a lumped thermal model[2] or spatially resolved thermal simulations to predict the cell temperature.[3,4] The reversible heat source term is at times ignored for high current applications (typically $\geqslant 1C$), however for mild to low C-rates ($\leqslant 1C$) the contributions from both terms are similar or higher, and the reversible heat flow term should be characterised and included.[5]

There are several factors that contribute toward the irreversible heat, they are all exothermic and are the i) electrolyte heat loss, ii) heat of mixing in the anode particles, iii) anode electrode Ohmic loss, iv) anode polarization loss, v) cathode particle heat of mixing, vi) cathode electrode Ohmic loss and vii) cathode polarization

loss.[6,7] More recent work also includes heat due to OCV hysteresis.[8] Characterising all these heat source terms is experimentally difficult, and often approximations are made when determining the irreversible heat.

In comparison, reversible heat exhibits both exothermic and endothermic behavior in different SoC regions. Figure 1 shows an example of a 21700 5Ah LGM 50 cell (NMC cathode and Si/C anode) undergoing a slow constant-current constant-voltage (CCCV) charge in a 25 °C thermal chamber.[9] Endothermic, "cooling" of the cell (by around 0.5 K) is visible, which cannot be explained if only the irreversible heat source is included.

The reversible heat arises due to the rate-of-change of entropy (S) of the electrodes, $\dot{Q}_{\mathrm{rev}} = -T dS/dt$ and is often approximated as

$$\dot{Q}_{\mathrm{rev}} = -T\frac{\mathrm{d}S}{\mathrm{d}t} \approx IT\frac{\partial U}{\partial T} \qquad [2]$$

with U being the cell open-circuit-voltage (OCV), T is the cell temperature (K) and I the cell current (A). The $\partial U/\partial T$ term in Eq. 2 indicates that the reversible heat is an electrode material property, and while both electrodes contribute to $\dot{Q}_{\mathrm{rev}}$, in this work we assume a single OCV case and do not split $\dot{Q}_{\mathrm{rev}}$ into a contribution from the anode and cathode (See[7] for the individual electrode contributions).

Of the two heat source terms discussed, it is the reversible heat source term that is of interest in this study, and in particular the $\partial U/\partial T$ term which we define here as the *entropy coefficient*. The entropy coefficient is a function of SoC, and it needs to be estimated for the full SoC range. Typically, the entropy coefficient is measured either with potentiometric or calorimetric approaches and with potentiometry often considered the reference approach, due to the experimental simplicity.

The principle idea of a calorimetric approach is to have a non-zero applied current and quantify, from the total heat, the amount of irreversible heat and reversible heat that is generated, and with the reversible heat quantified the entropy coefficient can be determined (via Eq. 2), see for example[10] and.[11] Calorimetric techniques however require prior knowledge about the cell thermal properties (heat capacity and thermal conductivity) and parameters contributing to the irreversible heat (e.g., the Ohmic resistance as a function of SoC), to arrive at $\dot{Q}_{\mathrm{rev}}$. Reliable estimates of these parameters are

[a]Now at Breathe Battery Technologies, United Kingdom
[b]Now at Dr. Ing. h.c. F. Porsche AG, Germany
[c]Now at Imperial College London, United Kingdom
[z]E-mail: Dhammika.Widanalage@warwick.ac.uk
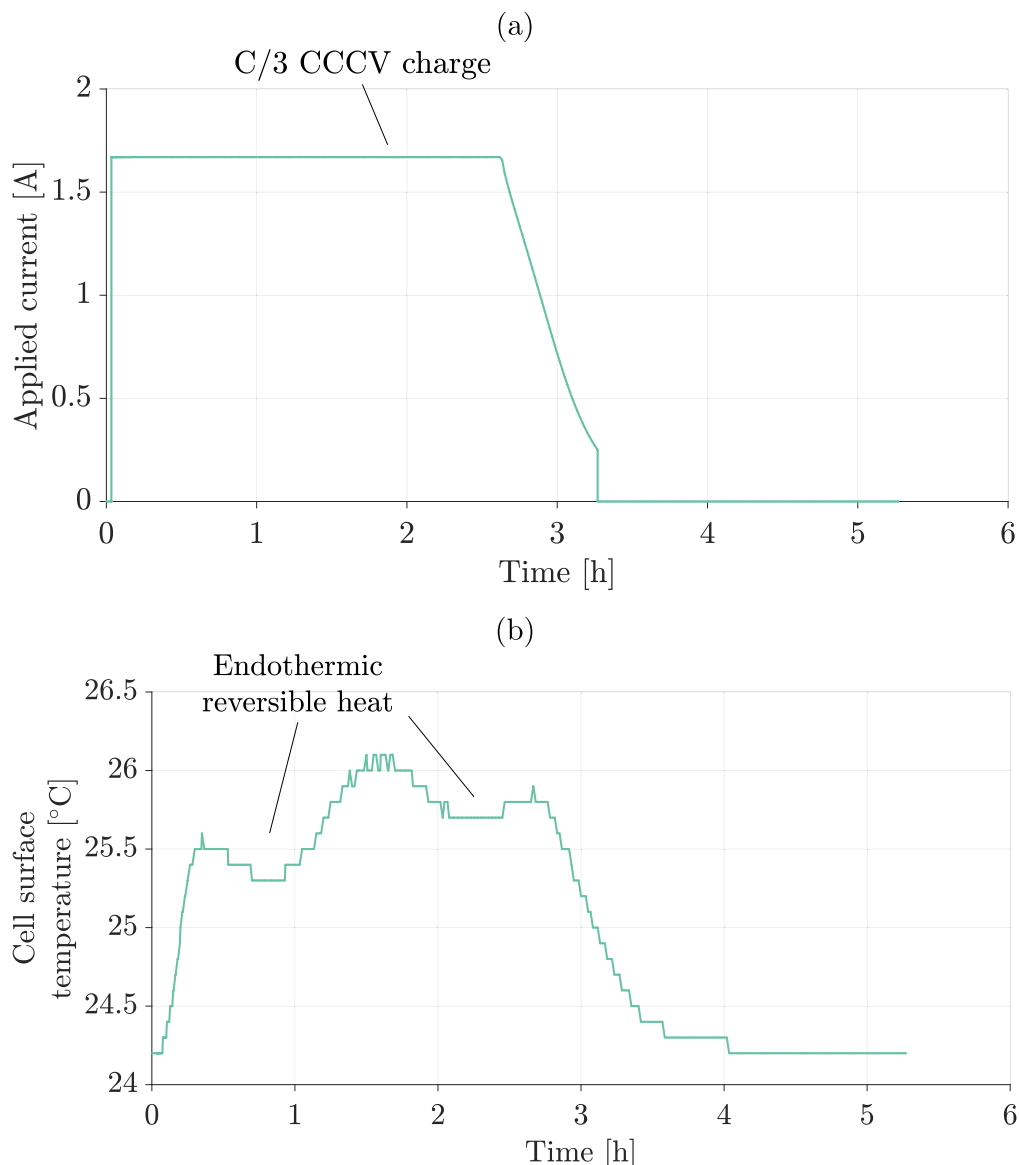
Figure 1. A C/3 CCCV charge current (a). Cell surface temperature response demonstrating reversible (endothermic) heat generation (b).

therefore important to obtain accurate entropy coefficient estimates in a calorimetric based approach.

The potentiometric approach, in comparison, does not rely on an applied current or a prior thermal model, but involves the application of step changes in temperature. This makes the procedure simple, however, it leads to considerably long experimental times, as the cell needs to equilibrate both thermally and electrochemically. Typical reported values includes 4 to 10 hours per step change[12] or 20 to 30 hours per SoC[11] or 5 to 17 hours per SoC as observed and presented later in this work. Hales et al.,[13] for example, accelerated the procedure with only one large temperature step at each SoC. Hu et al.[14] proposed a hybrid time-frequency method whereby a sinusoidal temperature signal is applied during the voltage relaxation phase. The excitation frequencies were chosen in such a way that a time reduction by a factor of ten, compared to a potentiometric method, was obtained but requires a correction to remove the voltage offset due to relaxation. See Zhang et al.[15] for a summary of the potentiometric techniques highlighting the trade-off between accuracy and measurement time.

Compared to existing techniques, where the entropy coefficient ($\partial U/\partial T$) is treated as determining an unknown *constant*, a more nuanced approach is considered here. The methodology developed here is more akin to the potentiometric approach, in that the applied current is zero, however we exploit the fact that the OCV is *dynamically* related to the cell temperature. The main contribution of the work is that we demonstrate how the entropy coefficient then manifests as the steady-state gain of this dynamical system. Using frequency domain system identification techniques, we develop a persistent temperature profile to perturb the cell and estimate the temperature-to-OCV dynamics; from which the entropy coefficient is obtained. The method has the advantage that it can account for transient OCV behavior and therefore strict OCV equilibrium is not required for each SoC stage. The procedure is termed here as the *kernel-based method* and the sections to follow detail the principle idea and methodology followed to test and validate the method.

Other frequency based approaches have been developed for entropy coefficient estimation, see for example.[11,12,16] However, these methods are in contrast to the frequency domain method presented here. Firstly, they are calorimetric based and therefore apply a non-zero current to heat the cell, rather than applying a persistently exciting thermal load. As stated earlier this requires quantifying the amount of irreversible and reversible heat that is generated. To this end, the methods exploit the relationship that the irreversible heat source term is non-linear with respect to the current

(quadratic) while the reversible heat source term is linear with respect to the current. As such by using a single frequency sinusoidal current (ω) only the reversible heat source term contributes to the fundamental frequency of the temperature response at ω, while the irreversible heat source term contributes to the 2nd harmonic of the temperature response at 2ω. Secondly, a thermal transfer function that maps the *reversible heat* to the measured *temperature* is required to calculate the reversible heat from the measured surface temperature, from which entropy coefficient can be determined; this differs with the kernel-based method, where a transfer function mapping the *temperature* to the *measured OCV* response is derived from which the entropy coefficient can be determined.

One such frequency domain method was developed in Ref. 11 with a sinusoidal current and then extended to separate the entropy coefficient to each electrode in Ref. 12 and more recently extended with a square wave current in Ref., 16 which improves upon the practicality over the use of a sinusoidal current. However, during the implementation of the methodologies some assumptions are not fulfilled, and further analysis into the approaches are required. For example, to expedite the experimental procedure a DC offset is added to the sinusoidal current in Ref., 11 as a result the irreversible heat will also contribute to the fundamental frequency of the temperature response at ω, and not only the reversible heat (and the separation of the heat source terms is no longer possible). Furthermore, the thermal transfer functions are a function of SoC, however in these methods, they are typically estimated for a single SoC (via a potentiometric approach[16]) and then used to derive the entropy coefficient for the entire SoC range. While such frequency based methods offer potential reduction in experimental time, further mathematical and experimental analysis is therefore required to determine the accuracy of the calorimetric frequency based approach.

Methodology and Experimental Setup

In this work, a system identification framework is followed (Fig. 2a) to determine the entropy coefficient. The approach involves the consideration of a model class ($\mathcal{M}$) to which the device-under-test belongs (a lithium-ion battery in this case), performing appropriate experiments ($\mathcal{X}$) to obtain the system response ($\mathcal{D}$), applying an identification routine ($\mathcal{I}$) to yield the model parameters, and finally, evaluating the validity ($\mathcal{V}$) of the estimated model. Should the estimated model fail at the validation stage, the model class and the data generating experiments have to be re-evaluated and the process repeated.

A schematic of how the battery is perturbed is shown in Fig. 2b. A reference temperature profile $T_{\text{ref}}(n)$, with $n = 0, 1, 2, \ldots,$ is applied to a Peltier element thermal controller (with a zero-order-hold (ZoH) inter sample behavior of hold Δt_{zoh} seconds) which creates a continuous-time temperature profile and controls the cell surface temperature (more details about $T_{\text{ref}}(n)$ is provided in the Experiments section and an example in the Results section). The measured cell surface temperature $T(t)$, and corresponding OCV response $U(t)$ are sampled with a sample rate of Δt seconds to generate the discrete-time data set $\mathcal{D} = \{T(t_n), U(t_n)\}$, with $t_n = n\Delta t$ and $n = 0, 1, 2, \ldots$ for the kernel estimation process.

The following subsections elaborate each of the system identification steps, which are then applied and demonstrated in the Results section.

Model class ($\mathcal{M}$) - Kernel function and parametric form.—

We start with the recognition that the relationship between the cell temperature and the cell OCV is dynamic in nature. This is understood through the observation that a step change in cell temperature leads to a gradual change in the cell OCV to a new steady-state OCV value, as is seen when performing potentiometric experiments (see for example Fig. 9a and further observations explained in the Supplementary material S1.2). Assuming that the temperature-OCV dynamics are linear, time-invariant, and stable, the
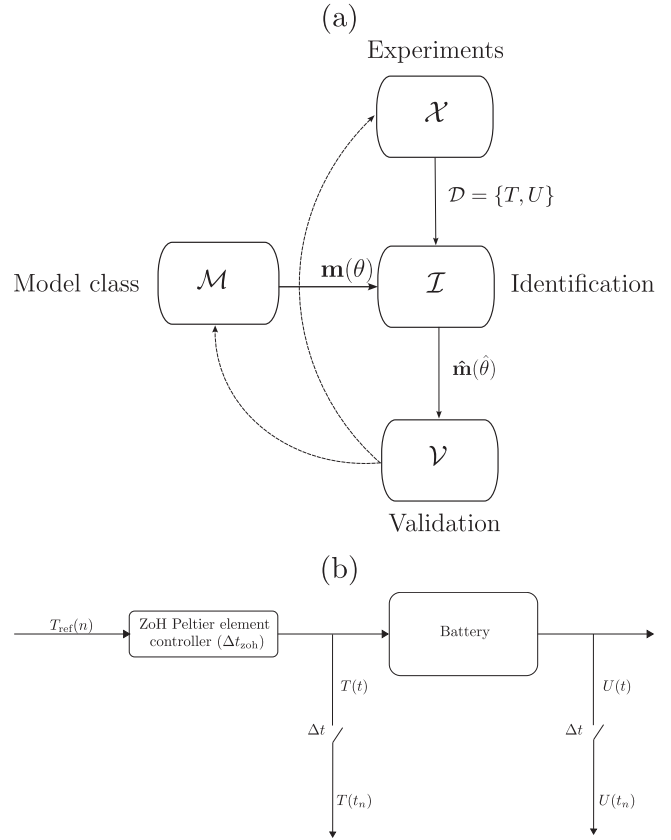
Figure 2. The typical system identification approach (a) and a schematic of how the battery temperature is perturbed (b). The process requires due consideration of the experiments ($\mathcal{X}$) to provide an input-output data set $\mathcal{D} = \{T(t_n), U(t_n)\}$, and a choice of the model class ($\mathcal{M}$) to which the physical system belongs. The application of the identification procedure, $\mathcal{I}$, then provides an estimate of the model candidate ($\hat{\mathbf{m}}(\hat{\theta})$), which upon validation may require changing the assumed model class or performing further experiments (denoted by the dashed line in Fig. 2a).

most general model class to predict the cell OCV is via a convolution of the cell temperature with a kernel function, as shown in Eq. 3.

$$U(t, z) = \int_{t_0}^{t_1} g(t - \tau, z) T(\tau) d\tau \quad t_0 \leqslant t \leqslant t_1 \qquad [3]$$

In Eq. 3, $U(t, z)$ is the OCV signal at a particular SoC (z), $T(t)$ is the cell temperature and $g(t, z)$ is the (unknown) kernel function (also known as the impulse response) relating the cell temperature to the OCV signal at that particular SoC. The time limit t_0 corresponds to a starting time instant where the cell is (ideally) at thermal and electrochemical equilibrium and the time limit t_1 corresponds to an end time instant over which $T(t)$ is applied.

The quantity of interest, however, is the entropy coefficient term $\partial U / \partial T$. By taking the derivative of Eq. 3[d] with regard to the cell temperature T it leads to

$$\frac{\partial U(z)}{\partial T} = \int_{t_0}^{t_1} g(\tau, z) d\tau. \qquad [4]$$

Since SoC is a given and can be treated as a constant while the temperature is changing, the unknown kernel function in Eq. 4 can be written as $g_z(t)$ implying that it is a function for a given SoC. Eq. 4 can then be written as

---

[d]Since we assume that the OCV-temperature kernel function $g(t, z)$ is time-invariant, but depends on SoC, $\partial U / \partial T$ can be written without an explicit dependence on time t.

$$\frac{\partial U}{\partial T} = \int_{t_0}^{t_1} g_z(\tau)\,d\tau. \qquad [5]$$

Equation 5 indicates that the entropy coefficient is simply the integral of the impulse response (at a particular SoC), which from linear system theory is known as the *steady-state gain* of the transfer function between, in this case, the cell temperature and the OCV response. If the dynamics are non-linear higher order kernels need to be included. The signal design and identification approaches discussed in the Experiments and Identification sections are designed such that non-linear effects are minimised and that a best-linear approximate (in the mean square sense) of the kernel function is obtained. This aligns with the potentiometric method which fits a linear relationship between the cell temperature and the OCV response. Similarly, if the dynamics are time-varying there would not be a steady-state gain and the entropy coefficient will be time-varying.

Estimating a transfer function of a dynamical system is a standard problem in system identification, and is typically *not* performed with step signals (as done when conducting potentiometric experiments), but rather with input signals that are more persistently exciting over a certain frequency bandwidth. A step signal can be understood as only perturbing a system at DC frequency ($f = 0$ Hz), while a persistently exciting signal perturbs the system at multiple frequencies allowing a transfer function to then be estimated. By estimating a transfer function of the OCV-temperature dynamics at higher frequencies, we can evaluate its steady-state gain[e], and from the interpretation of Eq. 5, this then is the entropy coefficient for that particular SoC.

In this work, we do not directly fit a transfer function to the input-output data $\mathcal{D} = \{T(t_n),\, U(t_n)\}$ (the cell temperature and the corresponding OCV response); instead, we first obtain a non-parametric estimate of the kernel function $g_z(t)$, in the frequency domain $G(\omega)$, with ω being the angular frequency (rad s^{-1}), and then parameterise $G(\omega)$ via a standard transfer function $G(s)$, with s the Laplace variable (Eq. 6).

$$G(s) = \frac{\sum_{m=0}^{n_b} b_m s^m}{\sum_{n=0}^{n_a} a_n s^n}. \qquad [6]$$

The non-parametric estimate $G(\omega)$ represents the frequency response between temperature and OCV, and estimating it first offers robustness when parameterising the model since it allows the necessary frequency components to be selected over which to parameterise $G(s)$. In Eq. 6, the coefficient a_0 is fixed to 1 while the model orders n_b and n_a are not predefined but found by solving a model order selection problem (by minimising the Akaike Information Criteria)[17,18,f].

Experiments ($\mathcal{X}$) - Signal design for kernel estimation.— Compared to the potentiometric method, several factors must be considered when designing the temperature signal for the kernel-based approach (for it to be a persistent excitation). The key difference is that the signal characteristics are considered in the frequency domain, while certain time domain constraints must be fulfilled such that the resulting signal can be realised via the Peltier elements of the thermal system. In practice, the temperature signal should not vary too rapidly and remain constant over the zero-order-hold (ZoH) duration (Δt_{zoh} seconds) of the Peltier controller, before either switching to a different value or remaining at the same temperature value (see Experimental setup section for further details). For a signal to be persistently exciting, it must inject power over the range of frequencies for which the dynamics are to be determined. We therefore start by considering the bandwidth (f_{min} to f_{max}) over which the temperature signal has to excite the battery OCV and then consider the amplitude spectrum of the signal.

In relation to the signal bandwidth, the minimum frequency (f_{min}) is dictated by the time duration (also known as the signal period) of the temperature signal (T_p), $f_{min} = 1/T_p$ Hz, and the maximum frequency (f_{max}) is an integer multiple of f_{min}, $f_{max} = K f_{min}$, as such the kth frequency between f_{min} to f_{max} is given as

$$f_k = k\, f_{min} \quad k \in H_{exc}. \qquad [7]$$

The value of K is the maximum number of harmonics that can be excited and is upper bounded by the Nyquist frequency, $f_{max} \leqslant 1/(2\Delta t_{zoh})$ to avoid signal aliasing. In Eq. 7, H_{exc} is the set of integer harmonics where signal power is present and can either take all values up to K, $H_{exc} = \{1, 2, 3, \ldots, K\}$, or only odd integers with all the even harmonics suppressed, $H_{exc} = \{1, 3, 5\ldots, K\}$, or a combination, whereby all even harmonics are suppressed and for instance harmonic multiples of 3 are furthermore suppressed, $H_{exc} = \{1, 5, 7, 11, \ldots, K\}$. There are benefits to the kernel estimation process in having harmonics suppressed, instead of injecting energy at all consecutive harmonics. The suppression of even harmonics minimises possible inter-hamornic modulation, should the OCV-temperature dynamics be non-linear, and will improve the estimation of $G(\omega)$. Such signal designs have been used in the literature for estimating current-voltage dynamics[19] and operando electrochemical impedance spectroscopy.[20]

The amplitude spectrum is governed by the desired temperature interval (T_{min} to T_{max}) and the number of discrete levels (L) the signal needs to cover. We start by assigning a unit amplitude over each harmonic in the set H_{exc} (a flat spectrum) and Schroeder phases ($\phi_k = -k(k-1)\pi/|H_{exc}|$) for each harmonic. For consecutive or odd only harmonics, Schroeder phases generate low crest-factor[g] signals and offers a good starting point for subsequent signal modification.[21,22] The signal is now fully defined in the frequency domain, a flat spectrum with Schroeder phases and a bandwidth from f_{min} to f_{max}, by taking the inverse Fourier transform (via the inverse Fast Fourier Transform) we then obtain a time-domain signal, which however will not span the desired temperature range (due to the unit amplitude spectrum). To achieve the desired temperature range, the resulting time signal is quantised into L levels and mapped to a corresponding L level sequence that spans T_{min} to T_{max} (Guidance for the temperature range is provided in the Discussions section). The resulting signal, known as the reference temperature signal $T_{ref}(n)$, will maintain a near-flat spectrum with any suppressed harmonics but will have out-of-band harmonics (energy beyond f_{max}) (due to the L-level signal quantisation). An example of a reference temperature signal $T_{ref}(n)$ with its specifications is shown in the Reference temperature profile section.

The OCV response is subsequently measured by applying this reference temperature signal at each SoC point (several periods of $T_{ref}(n)$ can be applied per SoC). The measured cell temperature ($T(t_n)$) and the corresponding OCV response ($U(t_n)$) form the input-output data set $\mathcal{D} = \{T(t_n),\, U(t_n)\}$ (as shown in Fig. 2a), which is then used to perform model identification.

Identification ($\mathcal{I}$) - Non-parametric frequency response and parametric transfer function estimation.—Rather than directly fitting a parametric transfer function (Eq. 6) to the experiment data set $\mathcal{D}$, we first obtain a non-parametric estimate of $g_z(t)$, in the frequency domain, followed by a parametric estimate. This intermediate step helps to derive more reliable estimates, since the fitting can be done on the excited frequency points (Eq. 7) while minimising any non-linear and noise contributions. Acknowledging that the temperature measurements will be imperfect (measurement noise) and that the OCV may not have reached steady-state (transient errors) with possible non-linear effects, an accurate relationship between the OCV response and the temperature signal, in the frequency domain, is as follows:

---

[e]The steady-state gain is the value of the transfer function at $f = 0$ Hz.
[f]The function `selstruc` from the MATLAB's `ident` toolbox is used for selecting the optimal model orders.

[g]The crest factor is an indication of the compactness of a signal. It is the ratio of the signal peak to the effective root-mean-square value of the signal over the frequency band of interest
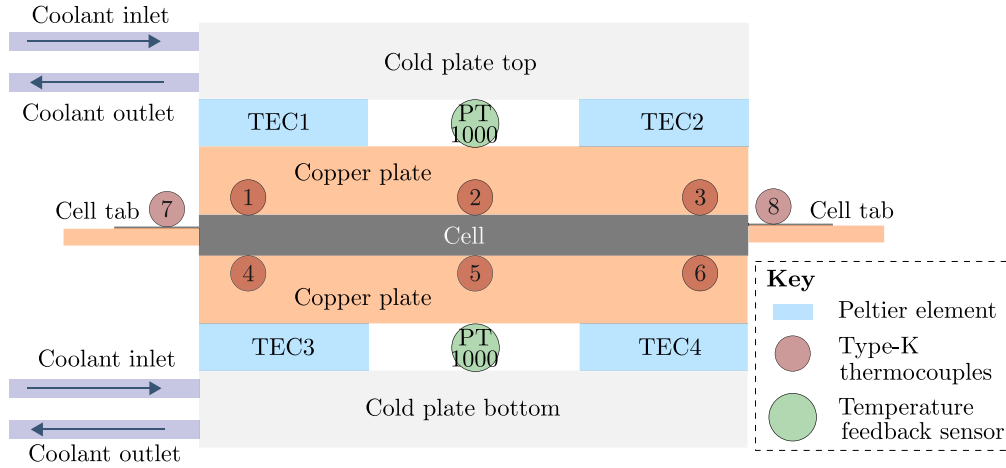
Figure 3. Schematic of the thermal rig used in the study.

$$U(\omega_k) = G(\omega_k)T(\omega_k) + H(\omega_k) + D(\omega_k) + E(\omega_k)$$
$$\omega_k = 2\pi k/T_p \quad k \in H_{exc} \qquad [8]$$

In Eq. 8, $G(\omega_k)$ is the temperature-to-OCV frequency response and is the (unknown) kernel function $g_z(t)$ (in Eq. 5) in the frequency domain. $T(\omega_k)$ and $U(\omega_k)$ are the Fourier coefficients of the temperature and OCV signals respectively. $H(\omega_k)$ is the transient error, $D(\omega_k)$ is any non-linear distortion error and $E(\omega_k)$ is the measurement noise, the effects of all of which should be minimsed when estimating $G(\omega_k)$. The suppression of even harmonics and the use of periodic signals (as described in the Experiments section) is motivated by this relationship, since such signals minimize the influence of $H(\omega_k)$ and $D(\omega_k)$.[22]

The classical approach of estimating $G(\omega_k)$, given $U(\omega_k)$ and $T(\omega_k)$, is by using window functions (such as a Hanning window) and computing the ratio between the windowed cross-power spectrum and auto-power spectrum (see[23–25]). Several advances in estimating frequency response functions with a low variance (compared to classical approaches) have been made and one such method is called the *Local polynomial method* (LPM),[26] which is employed in this work. In the LPM method a low-degree complex-coefficient polynomial (typically 2) is used to approximate the unknown frequency response ($G(\omega_k)$) and transient error ($H(\omega_k)$) in the neighborhood of each of the excited harmonics ($k \in H_{exc}$). The coefficients of the unknown polynomials then appear linearly, and by solving a linear least-squares problem for each harmonic in H_{exc}, a non-parameteric estimate of the frequency-response $\hat{G}(\omega_k)$ and its standard deviation ($\sigma_{\hat{G}}(\omega_k)$) is obtained (an estimate for the transient response $\hat{H}(\omega_k)$ is also obtained, but its value is not used any further). For a more detailed description of the LPM the reader is referred to,[26] and for its application in battery modelling please refer to.[27,28]

As a result of the LPM approach, the last design constraint on the temperature signal (together with the bandwidth and amplitude spectrum described in the Experiments section) is the number of harmonics that should be included in H_{exc} (which corresponds to the cardinality of the set H_{exc}). For a given complex-coefficient polynomial of degree d, the number of unknown coefficients that must be estimated is $2(d+1)$, which sets a lower bound on the number of harmonics as $|H_{exc}| \geqslant 2(d+1)$, and with $d = 2$ this means that H_{exc} should at least have six harmonics ($|H_{exc}| \geqslant 6$) to estimate the temperature-to-OCV frequency response while minimising any OCV transient errors. An example of a reference temperature signal that fulfills these conditions is presented in the Reference temperature profile section.

With the non-parameteric estimate of $\hat{G}(\omega_k)$ obtained (for a given SoC), we can now fit a parametric transfer-function by minimising

the following weighted cost-function.

$$\hat{\theta} = \arg\min_{\theta} \sum_{k \in H_{exc}} \left| \frac{\hat{G}(\omega_k) - G(\omega_k; \theta)}{\sigma_{\hat{G}}^2(\omega_k)} \right|^2 \qquad [9]$$

In Eq. 9, the definition of $G(\omega_k;\theta)$ is given in Eq. 6 with $s \equiv j\omega_k$ and θ corresponds to the transfer-function coefficients $\theta = [a_1, a_2,...,a_{n_a}, b_0, b_1,...,b_{n_b}]$. Equation 9 is non-linear in the parameters θ, for which a non-linear optimisaition routine is required, and we employed the Levenberg-Marquardt algorithm as the non-linear optimiser.

Once the optimal parameter set $\hat{\theta}$, per SoC is determined, the steady-state gain of the transfer function $G(s)$ (which is the entropy coefficient as shown in the Model class section) is obtained by setting $s = 0$. From Eq. 6 this corresponds to the ratio of b_0/a_0 and with a_0 set to 1 (as stated in the Model class section) the resulting entropy coefficient is simply the value of b_0, for that particular SoC.

Experimental setup.—The cell used in this study is a 3 Ah pouch cell (SLPB8043140H5, Kokam Co., Ltd.) with a NCA-LCO cathode and graphite anode.[29] The kernel-based method requires a setup capable of applying persistently exciting temperature profiles (as discussed in Secion 2.2). Therefore, a test setup with Peltier elements (ET-161-12-10-E, Adaptive® Thermal Management) was realised which enables temperature changes at a rate of >10 K s^{-1}. Figure 3 provides a schematic of the rig. Between each of the large cell surfaces and two Peltier elements, copper plates served as heat spreader. For evaluation, multiple calibrated 0.5 mm thermocouples of type K (ES Electronic Sensor GmbH) were placed in notches in the copper plate facing the cell surface and the feedback temperature for the Peltier elements was measured via a PT1000. The outward-facing side of the Peltier elements were connected to liquid cooling plates as heat sinks that were supplied with water from a cryostat (CC-K6s, Huber Kältemaschinenbau SE). The setup is symmetrical on both sides and the entire setup is compressed with springs for a constant pressure and positioned inside a insulated box.

Thermal equilibrium of 25 °C was ensured before the cell was charged with a CC-CV protocol (C/2, C/40 cutoff) to the upper voltage limit of 4.2 V with an HPS cyler from BaSyTec GmbH. Starting from 100 % SoC, the cell was discharged in 5 % steps of the measured nominal capacity to 0 % SoC with a C/2 current, giving 21 SoC break-points in total. At each of the SoC break-points, a potentiometric method is then conducted (the details of which are provided below) prior to the kernel-based method. The control of the temperature signal and voltage measurement (for both the potentiometric and kernel-based methods) was automated in LabVIEW (National Instruments). The Peltier element controllers (TEC16-24 KU2, head electronic) were also operated in this routine and the temperature and voltage measurement
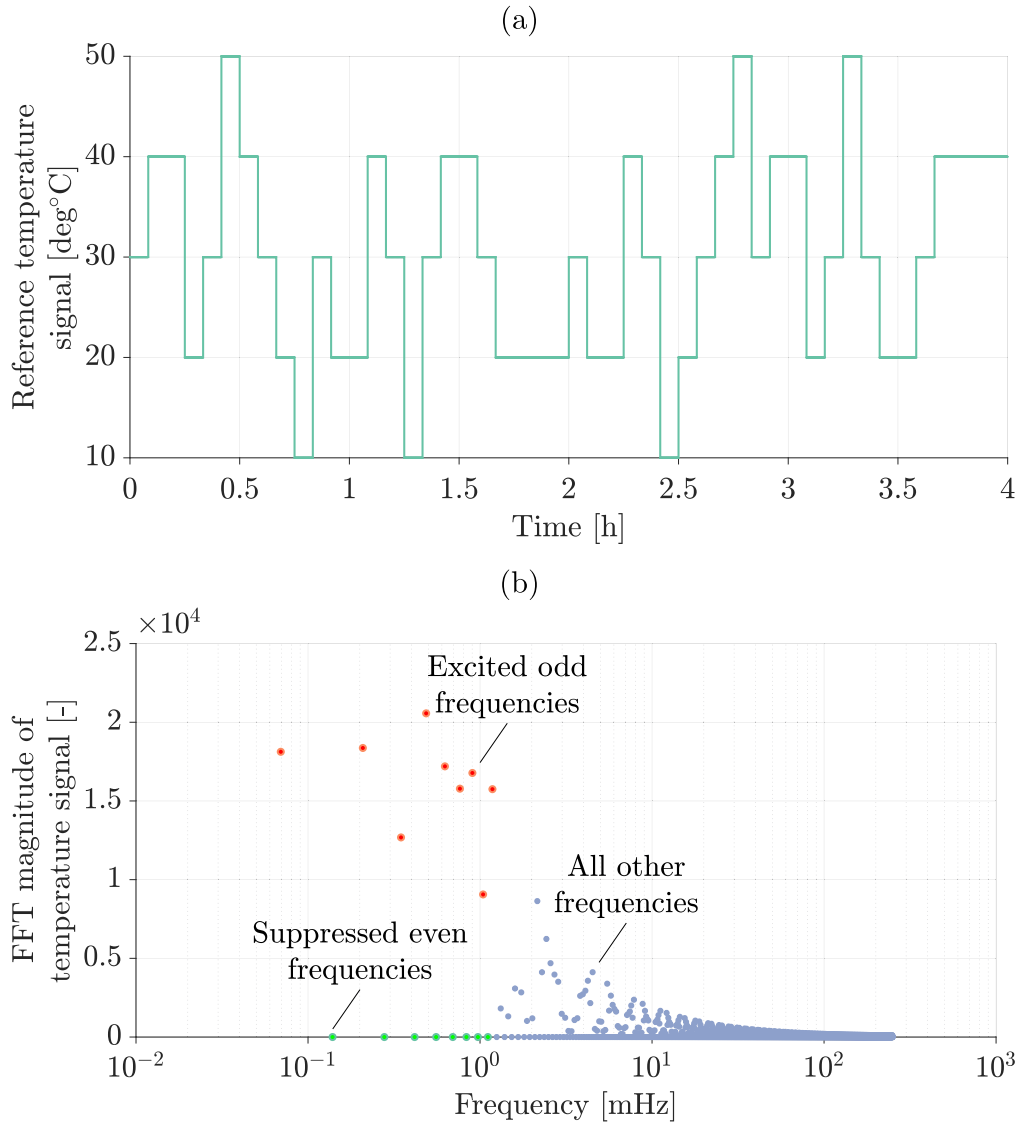
Figure 4. Reference temperature profile $T_{ref}(t_n)$ of period $T_p = 4$ hours and spanning five temperature level applied to the Peltier controller (a). The FFT magnitude of $T_{ref}(t)$ showing the excited odd harmonics with a fundamental frequency of $f_0 = 1/14400$ Hz and maximum excited frequency of $f_{max} = 1.2$ mHz and the suppressed even frequencies (b).

for evaluation was conducted with a multimeter (model 3706, Keithley Instruments, Inc.).

For comparison of the kernel-based entropy coefficient, at each of the SoC break-points, a standard potentiometric routine was performed before the kernel-based method was conducted. The same cell and the same test setup is therefore used, and both methods share the same SoC values. For the potentiometric method temperatures from 50 °C to 10 °C in 10 K steps were applied onto the cell while the voltage was measured. The rest time per potentiometric temperature step was event based. At least 1 h was allowed, however, thermal and electrical equilibrium were ensured with a further constraint that the changing rate falls below the threshold of 20 mK h^{-1} and 0.1 mV/h, respectively. However, at 100% SoC and high temperatures (50 °C) some self-discharge of the OCV was observed and the temperature set-point to 40 °C was done manually after a time period of 1.7 hours (See Fig. S9 in the Supplementary material).

Results

The various system identification stages, as described in the Methodology and Experimental setup section, are applied and the

Table I. The values used to generate the reference temperature signal $T_{ref}(n)$ for the kernel-based method.

Variable	Value	Description
T_{min}	10 ˚C	Minimum temperature
T_{max}	50 ˚C	Maximum temperature
L	5	Number of discrete temperature levels
T_p	4 h	Signal period
Δt_{zoh}	300 s	ZoH duration
Δt	2 s	Data sampling time
f_{max}	1.2 mHz	Maximum excited frequency
H_{exc}	{1,3,5,7,9,11,13,15,17}	Excited harmonic set

results of the intermediate stages leading up to the entropy coefficient result is given in the following subsections. As validation of the approach, the estimated entropy coefficients are compared against the potentiometric method. During the experiments of the kernel-based method three periods of the reference temperature
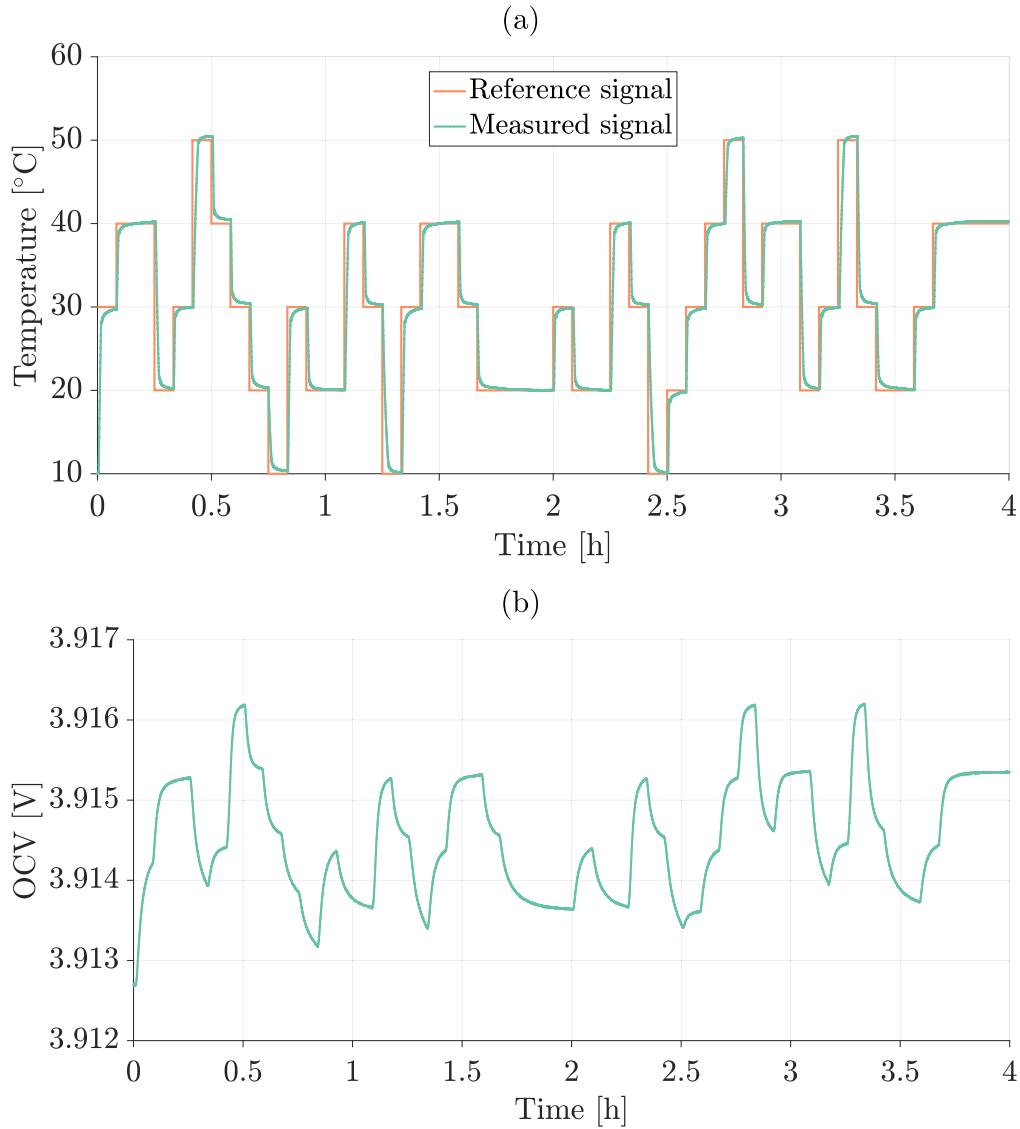
Figure 5. One period of the reference temperature $T_{ref}(t_n)$ (orange) applied at 80% SoC, and average measured cell surface temperature $\bar{T}(t_n)$ over thermocouples 1-6 (green) (a). The corresponding OCV response $U(t_n)$ at 80% (b).

profile were applied (as a form of redundancy and repeatability), however the analysis and results presented below are all based on the first period.

Reference temperature profile.—The details of the reference temperature signal $T_{ref}(n)$ used in this study are first presented. Through several evaluations, a signal period of $T_p = 4$ hours was found to be a suitable duration for the temperature signal (for each SoC point), which fixes the minimum frequency to $f_{min} = 1/T_p = 0.0694$ mHz (See the Discussions section for a further discussion on the choice of signal period). All even harmonics were suppressed up to $K = 17$, $H_{exc} = \{1, 3, 5, 7, 9, 11, 13, 15, 17\}$ (an odd harmonic signal) which results in $f_{max} = 17f_{min} = 1.2$ mHz and a cardinality of $|H_{exc}| = 9 \geqslant 6$. The signal was designed to cover a temperature range of $T_{min} = 10\,°C$ and $T_{max} = 50\,°C$ with $L = 5$ discrete levels. Each discrete temperature value was held for a minimum of $\Delta t_{zoh} = 5$ minutes before either switching or remaining at the same value. Table I summarises the parameter settings used to generate the reference temperature profile.

Figure 4a shows the samples of this reference temperature signal plotted against time ($T_{ref}(t_n)$ with $t_n = n\Delta t_{zoh}$) and the corresponding frequency domain plot is shown in Fig. 4b.

The frequency domain plot is obtained by computing the Fast-Fourier-Transform (FFT) of the reference temperature signal and the excited odd-harmonics, suppressed even-harmonics and the out-of-bound harmonics are explicitly labelled in the plot. This reference temperature profile was applied at each of the 21 SoC points, starting from 100% SoC to 0% SoC in steps of 5% SoC.

For a given SoC, the signal is applied to the Peltier element thermal controller (described in the Experimental setup section) with a sampling rate of $\Delta t = 2$ seconds. As stated in the Methodology and Experimental setup section, the analysis uses the *measured* cell temperature rather than the reference temperature. The average of the six thermocouples (labelled 1 to 6 in Fig. 3), corresponding to three on either side of the cell, is used to denote the measured cell temperature $\bar{T}(t_n)$.

Figure 5a shows one period ($T_p = 4$ hours) of the reference temperature, applied at 80% SoC and the corresponding (averaged) cell surface temperature ($\bar{T}(t_n)$) sampled every $\Delta t = 2$ seconds. The comparison shows good agreement between the reference and the measured average temperature, indicating good PID controller settings for the Peltier controller. This agreement ensures repeatability of the measurements and that the frequency spectrum of the measured signal is as close as possible to the reference signal that is elaborated below.
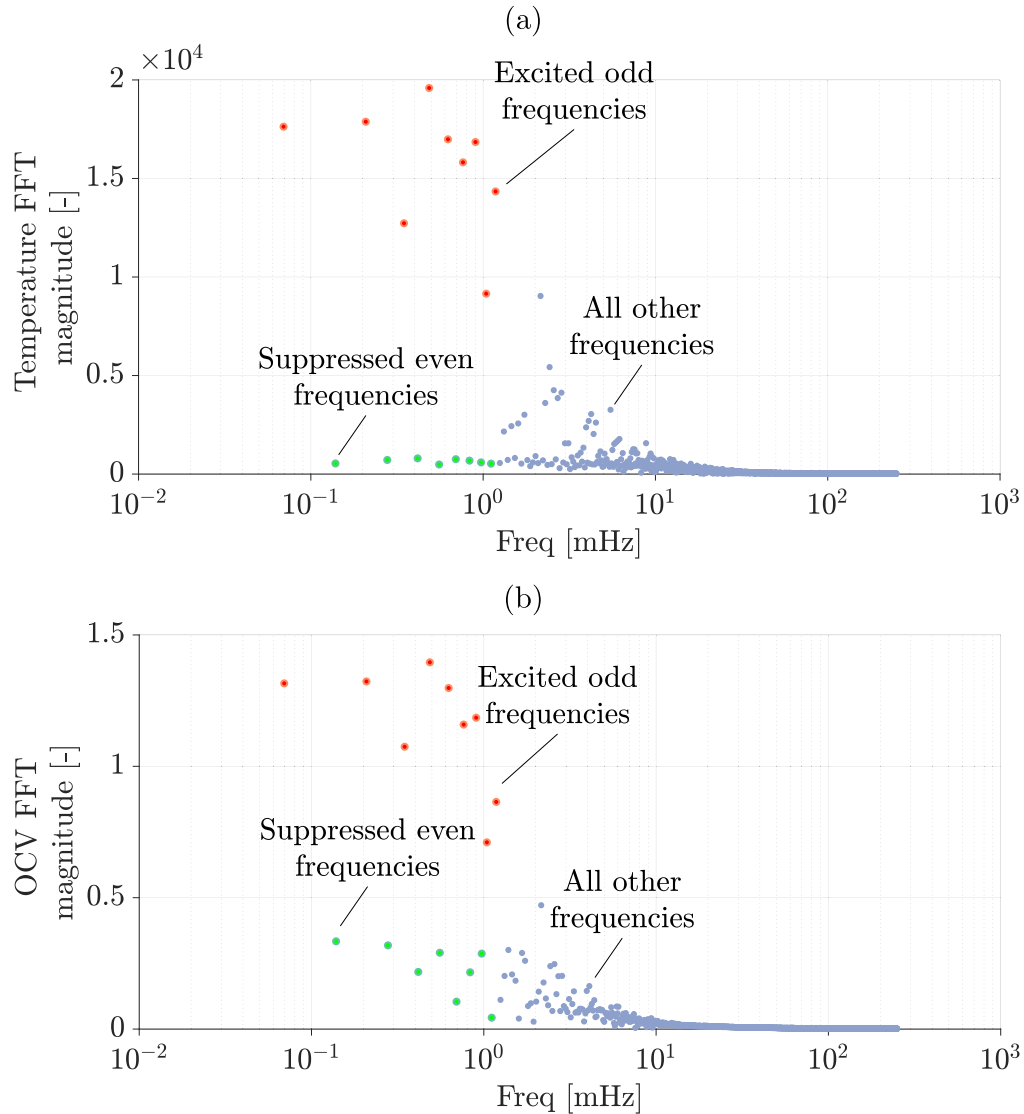
Figure 6. The FFT magnitude of the measured average temperature $\bar{T}(t)$ (a). FFT magnitude of the OCV response at 80% SoC (b). In both Figs. the harmonics indicate non-zero energy levels at the originally suppressed even harmonics (in relation to the reference signal) indicating side effects of the Peltier controller and transient with possible non-linear effects in the OCV signal.

The corresponding OCV response, over the 4 hours, is shown in Fig. 5b. The Fig. shows a clear dynamic behavior in the OCV response to the applied temperature and a peak-to-peak variation of approximately 3 mV is observed for a temperature change of 40 K.

As the subsequent analysis is performed in the frequency domain, the frequency content of the measured average temperature ($\bar{T}(t_n)$) and OCV response ($U(t_n)$) is provided in Fig. 6. The non-zero signal energy observed at the suppressed even-harmonics (in relation to the reference temperature profile, see Fig. 4b) indicates contributions from the Peltier controller. Ideally, if the Peltier PID controller yielded instantaneous responses, the suppressed even harmonics of the measured temperature (in Fig. 6a) will be zero. Similarly, the non-zero energy levels in the even harmonics of the OCV response (Fig. 6b) has contributions from the non-ideal Peltier controller, non steady-state OCV transient effects and possible non-linear distortions. If the OCV signal was at steady-steady and with no non-linear distortions, the suppressed even harmonics in Fig. 6b will also be exactly zero.

The excited-odd harmonics H_{exc} (indicated in Fig. 6) are then used to estimate the non-parametric frequency response and parametric transfer-function of the temperature-to-OCV dynamics, while

minimising the effect of transient errors (and possible non-linear distortions) as described in the Identification section.

Non-parametric response and parametric transfer function fit.—The non-parameteric frequency response, $\hat{G}(\omega_k)$, between OCV and temperature, is now estimated using the excited harmonic set in a given OCV response and average cell surface temperature (as shown in Fig. 6). This is achieved via the Local Polynomial Method (LPM) with a polynomial degree of 2 as described in the Identification section. The magnitude ($|\hat{G}|$), phase ($\angle\hat{G}$) and standard deviation ($\sigma_{\hat{G}}$) of the estimates as a function of frequency for 80% SoC is shown in Fig. 7. The standard deviation of the estimate (Fig. 7a) is approximately 20 dB lower denoting a high reliability of the temperature to OCV frequency response.

With the non-parametric frequency response in place, we parameterise it via a transfer function as explained in the Identification section, which subsequently will provide the entropy-coefficient for that particular SoC. Rather than prescribing a model order (values for n_b and n_a in Eq. 6) a model order sweep is performed (using Matlab's `selstruc` from the System Identification toolbox) that provides a good starting model order
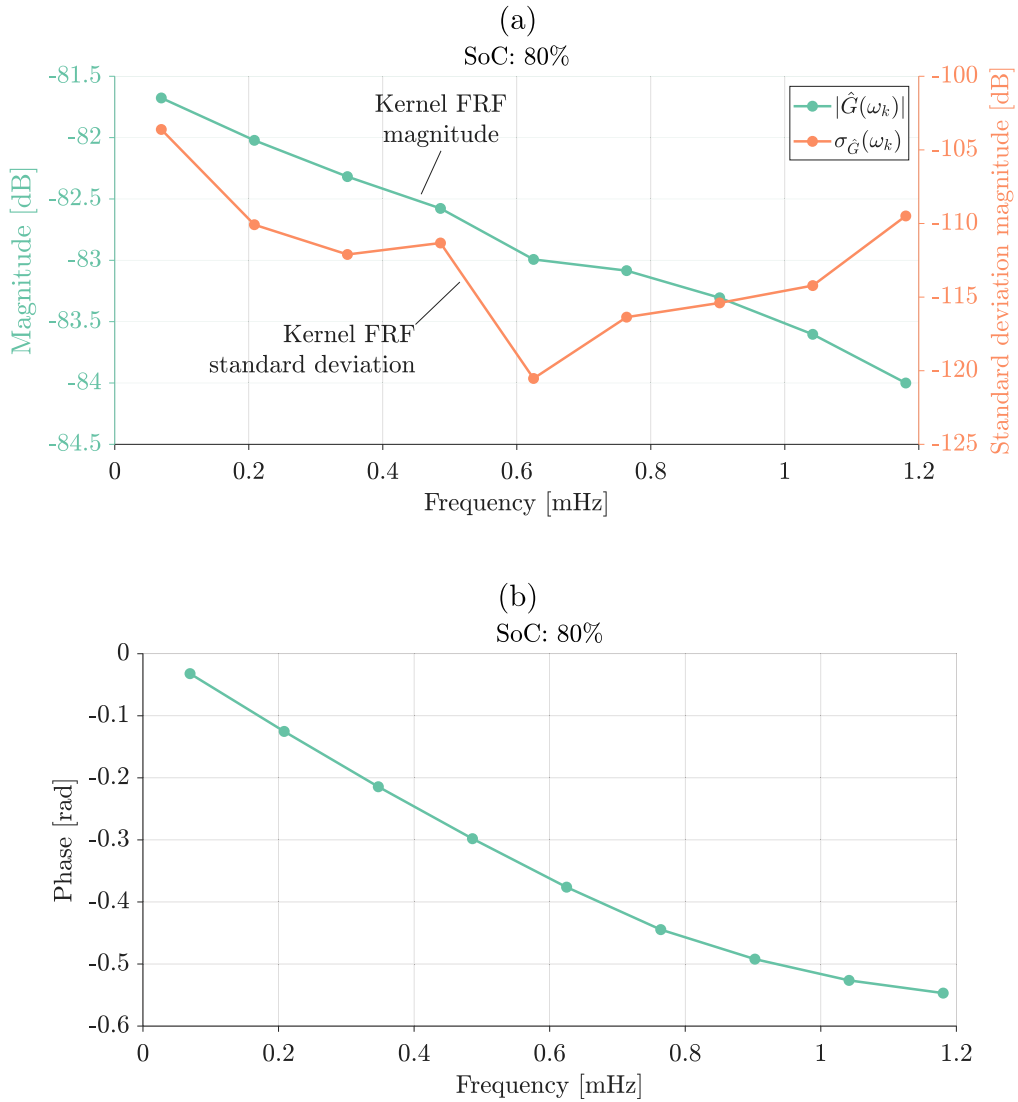
Figure 7. The estimated non-parameteric frequency response, $\hat{G}(\omega_k)$, at 80% SoC. The magnitude response (green) and the standard deviation (orange) (a). The phase response (b).

choice. For the example provided in Fig. 7 at 80% SoC, a model order of {1,4} was obtained, corresponding to numerator order of $n_b = 1$ and denominator order of $n_a = 4$. The corresponding transfer function fitted to the magnitude and phase response of $\hat{G}$ is shown in Fig. 8 (the transfer function fits for all other SoCs are provided in the Supplementary material Figs. S1 to S4).

Two error metrics were computed to evaluate the fitting performance. The corresponding fit had a Root-Mean-Square-Error (RMSE) value of 2.72E-6V/K and a Goodness-of-Fit (GoF) of 99.6% that indicated an agreeable transfer function fit. The entropy coefficient is then obtained by reading the numerator coefficient value b_0 (see the Identification section). For this example, at 80% SoC, the value of b_0, and therefore the entropy coefficient, is 0.082 ± 0.002 mV K^{-1}. The standard deviation of the estimate is approximated via the Jacobian matrix obtained at the termination point of the non-linear least squares optimisation ($\sigma_\theta^2 \approx \mathrm{diag}((J^T J)^{-1})$).

Table II provides the complete set of fitting metrics for the transfer functions and subsequent kernel-based entropy coefficient estimates for the 21 SoC points. The last step of the system identification procedure corresponds to the validation of the values presented in Table II. For this we use the results of the potentiometic based entropy coefficient estimation and compare the results against the kernel-based approach.

Comparison and validation with the potentiometric method.— The potentiometric method is also performed across the same 21 SoC points, with a starting temperature of 50 °C and going down to 10 °C in steps of 10 K. As mentioned in the Experimental setup section the time duration for each temperature step change was not fixed but was at least 1 hour or terminated when the rate of change of voltage was less than 0.1 mV K^{-1} and the rate of change of cell surface temperature was less than 20 mK h^{-1}.

Figure 9a shows the temperature profile and corresponding OCV response for the potentiometric method when the cell is at 80% SoC. The analysis and derivation of the entropy coefficient term for the potentiometric method is a lot simpler compared to the kernel-based approach. Once both the cell surface temperature and OCV equilibrate the steady-state values are read off (these are marked with a × marker in Fig. 9a) and plotted against each other (as shown in Fig. 9b). The gradient of the straight line fit is then the entropy coefficient $\partial U/\partial T$ term. For the example shown in Fig. 9 value of $\partial U/\partial T = 0.088 \pm 0.001$ mV K^{-1} is obtained, which is comparable to the value of 0.082 ± 0.002 mV K^{-1} obtained from the kernel-based approach.

Table III provides the complete list of the entropy coefficient values, and its standard deviation, for the potentiometric method at all 21 SoC points. The RMSE and GoF values are also provided together with the total testing time duration that was required per SoC.
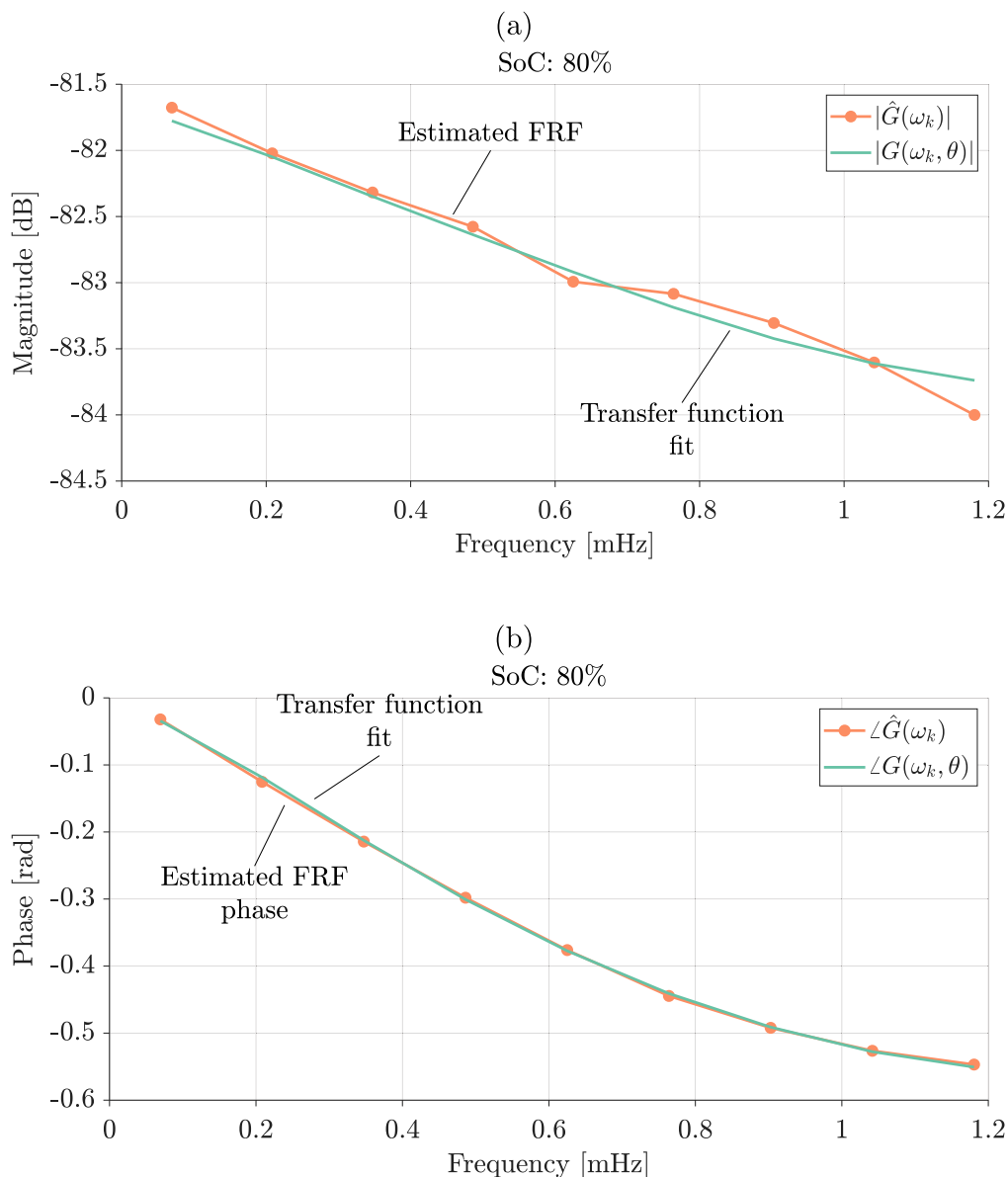
Figure 8. A fourth order transfer function fit of the estimated non-parameteric frequency response at 80% SoC. The estimated magnitude response (orange) and transfer function fit (green) (a). The phase response (orange) and transfer function fit (green) (b). A total test time duration of 4 hours was required and resulted in $\partial U/\partial T = 0.082 \pm 0.002$ mV K^{-1}.

As validation of the kernel-based method, we can compare the entropy coefficient values in Table II against Table III, which indicates good agreement in the results. A plot of the values is also provided in Fig. 10, that shows how the kernel-based method gives equally comparable results as that obtained from the potentiometric method, demonstrating the validity of the method.

Discussions

Comparison of the methods.—For both approaches the entropy coefficient is negative except between, approximately, 65% to 95% SoC where it becomes positive. Depending on the convention adopted, the sign change indicates an interval of either an exothermic or endothermic reversible heat generation. In this paper, positive current is taken to be charging, resulting in exothermic heat generation being positive and endothermic heat generation being negative. As such, while charging from 0% SoC, the cell will undergo endothermic reversible heat from 0% to around 65% SoC and then exothermic reversible heat from around 65% to 95% SoC

before becoming endothermic again from 95% to 100% SoC. This process changes for a discharge current (65% to 95% SoC is endothermic while all other SoC intervals become exothermic). The measured entropy coefficient is in line with the entropy coefficient measured on a NCA-LCO graphite cell of the same cell manufacturer.[11] The cathode active material of this cell (as stated in the Experimental setup section) is a blend of LCO and NCA and the entropy coefficient of blended materials is influenced by both the corresponding constituents. This has been studied using mixed potential theory by Huang et al.,[30] and the estimated entropy coefficient can be attributed primarily to the NCA material.

The potentiometric responses for all the remaining SoC points are provided in the Supplementary material (Figs. S5 to S9). The OCV response demonstrates an interesting behavior around 65% and 95% SoC where the entropy coefficient undergoes a sign change (Fig. S8 and S9). In these SoC intervals the OCV either overshoots before reaching steady state, indicating a strong higher order (> 1) dynamical behavior or undershoots in the opposite direction before reaching steady state, indicating a non-minimum phase behavior

Table II. The transfer function fitting metrics across all the SoCs and the corresponding kernel-based entropy coefficient and standard deviation. The model order corresponds to the numerator and denominator orders. The SoCs denoted with an asterisk (*), indicate cases where the frequency range was manually reduced to fit the first five harmonics and the model orders were manually set to improve the GoF.

Transfer function metrics					Entropy coefficient	
SoC [%]	GoF [%]	RMSE [V K^{-1}]	Model order $\{n_b, n_a\}$ [-]	Duration/SoC [h]	$\partial U/\partial T$ [mV K^{-1}]	Std. $\partial U/\partial T$ [mV K^{-1}]
0	99.6	2.44E-06	{3,1}	4.0	−0.387	0.0004
5	99.9	1.08E-06	{3,1}	4.0	−0.336	0.0002
10*	68.6	2.79E-06	{2,3}	4.0	−0.085	0.0014
15	76.2	1.51E-05	{1,2}	4.0	−0.178	0.0047
20*	98.0	6.32E-07	{2,3}	4.0	−0.087	0.0042
25*	98.7	1.23E-06	{2,3}	4.0	−0.105	0.0135
30*	60.1	1.50E-06	{2,3}	4.0	−0.338	0.0084
35	88.3	1.71E-05	{2,2}	4.0	−0.498	0.0061
40	99.3	8.18E-06	{2,2}	4.0	−0.555	0.0013
45	99.1	8.79E-06	{2,3}	4.0	−0.478	0.0023
50	70.7	2.15E-05	{1,2}	4.0	−0.218	0.0076
55	61.0	2.35E-05	{1,2}	4.0	−0.139	0.0057
60	81.7	1.65E-05	{1,2}	4.0	−0.065	0.0030
65	95.7	8.80E-06	{1,2}	4.0	−0.015	0.0011
70	98.3	5.72E-06	{3,1}	4.0	0.027	0.0009
75	99.0	4.38E-06	{3,1}	4.0	0.059	0.0008
80	99.6	2.72E-06	{1,4}	4.0	0.082	0.0017
85	98.4	5.61E-06	{1,2}	4.0	0.115	0.0010
90	77.5	1.76E-05	{1,2}	4.0	0.138	0.0026
95*	96.5	5.04E-06	{2,3}	4.0	−0.010	0.0160
100	83.5	1.17E-05	{1,2}	4.0	−0.054	0.0018

with regards to temperature. While we note these observations here, it is necessary to separate the OCV-temperature dynamics to the individual electrodes to identify the contributing factors to this behavior.

In this work, the SoC direction for both potentiometric and kernel-based methods was from high SoC (100%) to low SoC (0%). To characterize any hysteresis effect of OCV on the entropy coefficient estimates, the experiments would need to be repeated in the increasing SoC direction as well (from 0% SoC to 100% SoC). This, however, will at least double the experimental time and the improvement in any subsequent thermal simulations (with a direction-dependent entropy coefficient curve) is unclear. If a direction-dependent entropy coefficient curve is required, neither the potentiometric nor the kernel-based approach is recommended due to the long experimental time and a calorimetry-based method should be investigated (such as the one presented in Ref. [11])

Improved OCV models.—As discussed in the introduction, determining the entropy coefficient is motivated in the context of improving thermal simulations, since it quantifies the reversible heat source term. However, entropy coefficients can also be used as a diagnostic tool to identify electrode defects and provide degradation markers [31,32] or to study voltage hysteresis [33,34]. The kernel-based method can similarly offer potential improvements to OCV modelling of a lithium-ion battery. Given that the measured terminal voltage is dominated by the OCV (typically by around 95%), developing more accurate SoC and temperature dependent OCV models is highly beneficial.

A first approximation of an OCV model is to assume no dynamics and model $U(z, T)$ as a first order Taylor approximation, as shown in Eq. 10.

$$U(z, T) \approx \bar{U}(z) + T\frac{\partial U}{\partial T}\bigg|_z \qquad [10]$$

In Eq. 10, $\bar{U}(z)$ is the OCV at a given SoC (assuming no hysteresis) and $\frac{\partial U}{\partial T}\big|_z$ is the entropy coefficient, at that SoC. The entropy

coefficient estimated via a potentiometric or kernel-based method can be used in this OCV model. The $\bar{U}(z)$ term can either be a linear interpolation function or a parametric MSMR (multi-species multi-reaction) model.[35]

In the kernel-based method, we however, also obtain the dynamics of the temperature-to-OCV response (in the form of the transfer function $G(s)$). By converting it to a time-domain state-space representation, we can add dynamics to the OCV model as shown in Eqs. 11 and 12.

$$U(z, T) \approx \bar{U}(z) + \Delta U(T) \qquad [11]$$

$$\frac{d\Delta U}{dt} = A_z \Delta U + B_z T(t) \qquad [12]$$

In Eq. 11, $\Delta U(T)$ is the deviation from the OCV at a given SoC and is now a *solution* to a linear differential equation given in Eq. 12. Here, A_z and B_z are the state-space matrices of the transfer function $G(s)$ at a particular SoC. Hysteresis dynamics can be accounted by adding a one-state hysteresis to $\bar{U}(z)$[8,36] or through formulations based on phase change models, for example.[37]

Thorough experimental validation of these models is however required, since both Eqs. 10 and 11 assume a linear combination of the SoC and temperature OCV dependence. Much work is still required in developing *dynamic* OCV models that account for both SoC and the temperature of the cell.

Practical aspects of the kernel-based method.—It is worth elaborating on the practicalities of the kernel-based method. Compared to the potentiometric method, there is more signal processing overhead with the kernel-based method, however, from a user perspective once the temperature and OCV data are collected the processing can be automated and done through robust software code, making the analysis easier. A Matlab code base that generates the temperature signals in the frequency domain and performs the analysis discussed here is shared via a GitHub link at the end of the paper (the code base also includes the experimental data set and a
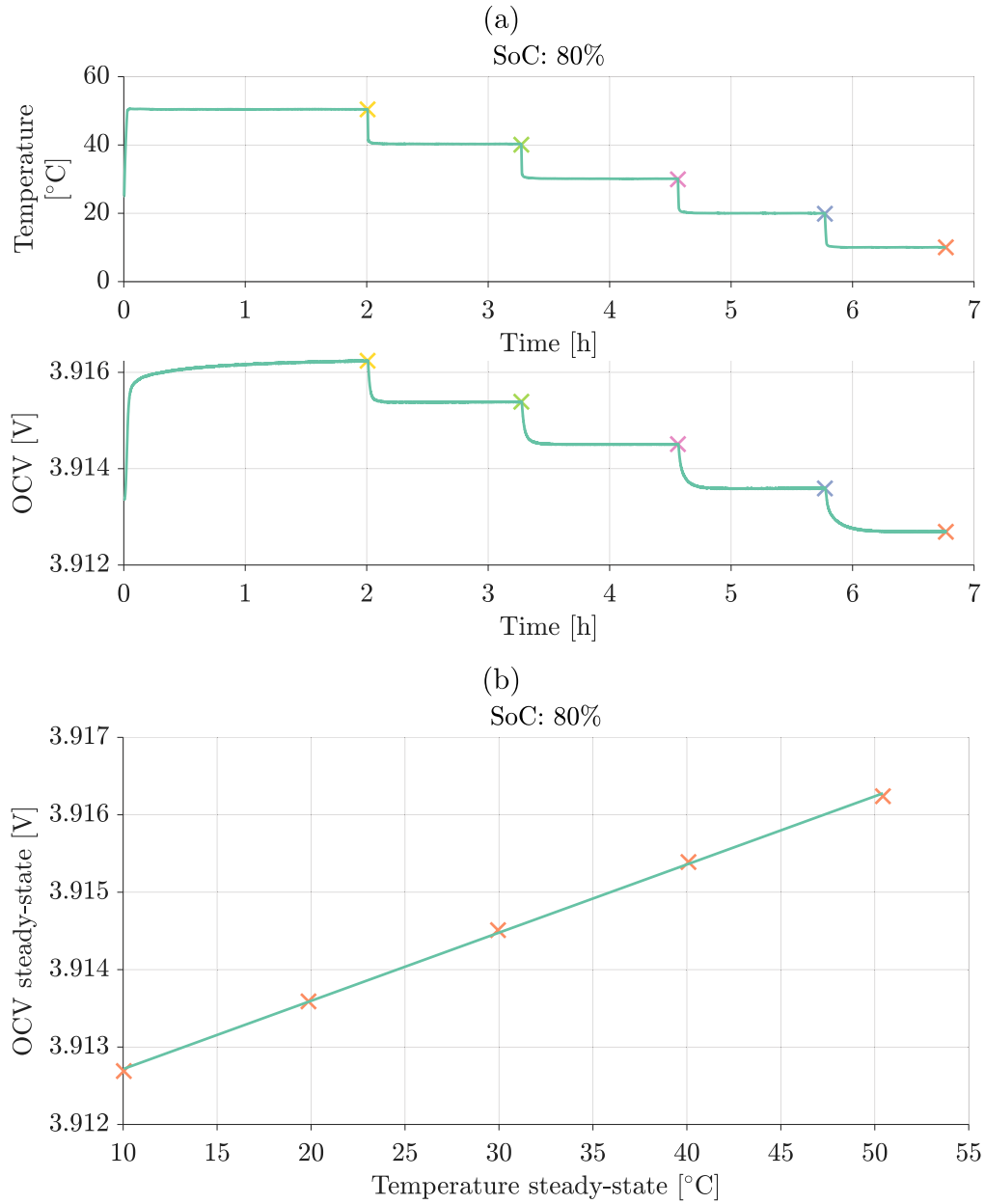
Figure 9. The cell temperature and OCV response for the potentiometric method at 80% SoC. Markers (×) denote the point considered as steady-state (a). Potentiometric straight line fit for 80% SoC at steady-state conditions (b). A total time duration of 6.8 hours was required for the five temperature step changes and resulted in $\partial U/\partial T = 0.088 \pm 0.001$ mV K^{-1}.

script that an interested reader can use to reproduce all the results presented in this paper).

The parameter settings for the reference temperature signal (as given in Table I) also require some guidelines, in particular the temperature range parameters T_{min} and T_{max}, the time based parameters Δt_{zoh} and T_p, and the frequency range parameters f_{min} and f_{max} (or H_{exc}).

A large temperature range ($\geqslant 20$ K) is desirable, given the sub mV per Kelvin variation in OCV, to amplify the OCV response and improve the signal-to-noise ratio. It is however recommended to keep $T_{max} \leqslant 50$ °C to avoid accelerated degradation and $T_{min} \geqslant 0$ °C for ease of the Peltier control.

The value of Δt_{zoh} is guided by the cell thermal inertia and should be set such that the temperature gradient induced within the cell should be a minimum (at the end of the Δt_{zoh} interval). By doing so the average measured temperature ($\bar{T}(t_n)$) will be a fair representation of the cell and be can be associated with the OCV response. If

the specific heat-capacity (C_p) and through plane thermal-conductivity (κ) of the cell are known, Δt_{zoh} can be set to be larger than the characteristic timescale of the cell thermal diffusivity as

$$\Delta t_{zoh} > L_c^2/D \quad \text{with}$$
$$D = \kappa/(\rho C_p). \quad [13]$$

In Eq. 13, L_c is the cell thickness and ρ is the cell density. For the cell studied in this work, $\kappa = 0.86$ W/m/K, $\rho = 2.89$E3 kg m^{-3}, $L_c = 75$ mm and $C_p = 789.7$ J/kg/K, giving a characteristic diffusion timescale of 149.5 seconds and the value of Δt_{zoh} was set to 300 seconds fulling the condition in Eq. 13. A simulation of the cell inner/midpoint temperature (at $L_c/2$) is shown in Fig. S11 of the Supplementary material. It demonstrates how the inner temperature reaches the average temperature measured at the boundaries within the $\Delta t_{zoh} = 300$ s interval; indicating a minimum thermal distribution within the cell.

Table III. The potentiometric fitting metrics across all the SoCs and the corresponding entropy coefficient and standard deviation. The 100% GoF values are an outcome of rounding the values to the nearest decimal.

| SoC [%]	GoF [%]	RMSE [V]	Duration/SoC [h]	$\partial U/\partial T$ [mV K^{-1}]	Std. $\partial U/\partial T$ [mV K^{-1}]
0	100.0	1.20E-04	17.1	−0.385	0.002
5	100.0	8.93E-05	13.9	−0.337	0.002
10	99.2	1.90E-04	5.0	−0.066	0.003
15	99.3	4.74E-04	14.6	−0.172	0.009
20	99.3	2.59E-04	13.5	−0.098	0.005
25	99.2	4.06E-04	16.4	−0.142	0.007
30	99.6	6.78E-04	7.0	−0.341	0.012
35	99.9	5.47E-04	8.9	−0.497	0.010
40	100.0	1.47E-04	6.9	−0.568	0.003
45	100.0	1.01E-04	14.6	−0.507	0.002
50	100.0	1.19E-04	8.0	−0.227	0.002
55	99.9	1.44E-04	7.7	−0.138	0.003
60	99.2	1.60E-04	6.6	−0.057	0.003
65	39.3	8.72E-05	8.4	−0.002	0.002
70	99.0	1.24E-04	6.4	0.038	0.002
75	100.0	4.88E-05	6.9	0.069	0.001
80	99.9	6.50E-05	6.8	0.088	0.001
85	99.3	3.37E-04	5.9	0.123	0.006
90	97.6	7.54E-04	6.6	0.150	0.014
95	93.3	4.08E-04	6.5	−0.048	0.007
100	99.4	1.09E-04	6.3	−0.044	0.002

The value of the signal period, T_p, is guided by the OCV-to-temperature dynamics. If T_p is set very low (e.g., in the order of minutes) the variation of OCV will be in the sub millivolts and high precision voltage sensors will be required to measure the response. Increasing T_p is beneficial in that $f_{\min}=1/T_p$ will reduce, aiding the steady-state response, but this is then at the expense of increasing the experimental time. Since the OCV-to-temperature dynamics are unknown, through an initial phase of trial-and-error we found 4 hours to excite low frequency dynamics well. Section S1.4 of the Supplementary material provides early stage results and analysis of using $T_p = 2$ h. The estimated frequency response, when at 50% SoC, is shown in Fig. 2. The estimated entropy coefficient values are

similar with a higher standard deviation for $T_p = 2$ h (Table S2) however the ZoH duration, sampling time and temperature limits were not finalised. Given the similarity of the results, a value of $T_p = 2$ h may act as a good starting point for any subsequent new chemistries together with the signal guidelines provided in this section.

With the frequency bandwidth based parameters $f_{\min}$ is not a free variable and is constrained by the guidance of T_p, $f_{\min}=1/T_p$ (as described in the Experiments section). The maximum frequency is however a free variable but is still bounded. On the lower end $f_{\max}=K f_{\min}$ with $K \in H_{\text{exc}}$ and $|H_{\text{exc}}| \geqslant 6$ (as described in the Identification section) and on the upper endothermic $f_{\max} \leqslant 1/(2\Delta t_{\text{zoh}})$ which is the Nyquist frequency to prevent any aliasing. The GitHub code base includes a signal generation routine that helps the user to generate a reference temperature signal conforming to these requirements and informing of any constraint violation and how to adjust the parameters to meet the constraints.

One major practical limitation of the kernel-based method is the need for a specialist thermal rig. Convection based thermal chambers, typically used during battery testing, cannot be used to emulate the reference thermal profile required for the method (Fig. 4a). Further work is therefore required to validate the kernel-based method across different cell form factors with appropriate Peltier rig designs to control the cell surface temperature.

From a time-per-SoC perspective, the kernel-based method has an advantage since it is not necessary for the OCV to reach steady-state, while for potentiometric methods steady-response is crucial. Referring to Table II the kernel-based method required 84 hours (4 hours/SoC × 21 SoC points), while from Table III the potentiometric method required 194.3 hours (the sum of the Duration/SoC column), which is a 57% time reduction. The Supplementary material S1.2 provides results of the potentiometric method if only the first three temperature set-points per SoC are used, which is the minimum number of temperature set-points required for a potentiometric method. Some deviation is observed for SoCs between 15% to 40% and 90 % SoC, with good agreement over the remaining SoC points. Using only three temperature set-points reduced the total time to 142.2 hours (from 194.3 hours), which still corresponds to a 69 % higher time duration than the kernel-based method. Three temperature set-points per SoC is the minimum number required for the potentiometric method however for robust estimates, as observed in Fig. S10, four or five temperature set-points per SoC are recommended.
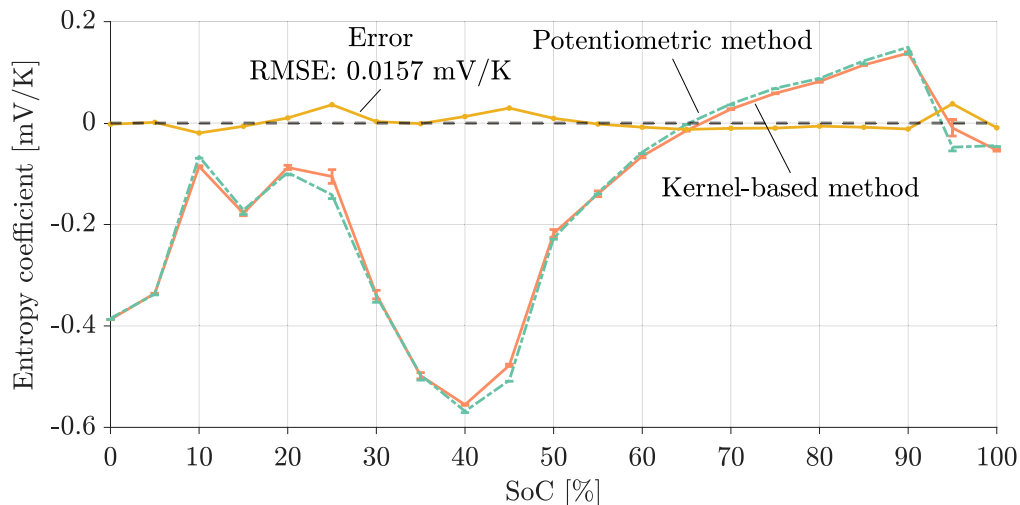
Figure 10. Comparison of the kernel-based (orange) and potentiometric (green) based entropy coefficient estimation together with the standard deviation estimate and the error between the kernel-based and potentiometric method (yellow). The plot shows a good agreement between the two approaches and thereby validating the kernel-based method for the NCA-LCO cathode and graphite anode 3 Ah battery. The dashed line indicates the zero line to denote positive and negative entropy coefficients intervals.

Conclusions

The paper demonstrated that the steady-state gain of the transfer function (from temperature to OCV) corresponds to the entropy coefficient. The relationship between the entropy coefficient and the integral of the impulse response (termed here as the kernel function between the OCV and cell temperature dynamics) was established. This relationship was exploited and validated by following a system identification procedure, namely in the frequency domain. By thermally perturbing the battery at high frequencies, the time required to infer the dynamics is reduced, while being able to infer the steady-state gain (at $f = 0$) through an appropriate parametric transfer function.

The approach has an advantage in that it can accommodate for non steady-state OCV transient effects. This is achieved by accounting for a transient term in the frequency domain when relating the temperature-to-OCV dynamics. However, the approach relies on a thermal rig that can apply a persistently exciting thermal profile, which can act as a practical limitation for its implementation.

Theoretical concepts were experimentally validated by estimating the entropy coefficient of a NCA-LCO cathode and graphite anode 3 Ah pouch cell. The entropy coefficient was estimated over 21 SoC points and compared against a potentiometric approach and showed very good agreement across the entire SoC interval with a 57% reduction in time.

Acknowledgments

Data and code availability

The data and the code to reproduce all the results presented are available at the following repository https://github.com/WDWidanage/Entropy_Coefficient_Estimator.

Examples of how to generate a persistently exciting thermal profile and perform analysis (if a compatible thermal rig is present) are also provided in the repository.

ORCID

W. D. Widanage ⓘ https://orcid.org/0000-0003-0428-2554
O. Queisser ⓘ https://orcid.org/0000-0003-1653-4683
S. Paarmann ⓘ https://orcid.org/0000-0003-1629-6830
L. Cloos ⓘ https://orcid.org/0009-0006-1001-2891

References

1. M. Doyle, T. F. Fuller, and J. Newman, "Modeling of galvanostatic charge and discharge of the lithium/polymer/insertion cell." *J. Electrochem. Soc.*, **140**, 1526 (1993).
2. F. Brosa Planella, M. Sheikh, and W. D. Widanage, "Systematic derivation and validation of a reduced thermal-electrochemical model for lithium-ion batteries using asymptotic methods." *Electrochimica Acta*, 138524 (2021).
3. J. Sturm, A. Rheinfeld, I. Zilberman, F. B. Spingler, S. Kosch, F. Frie, and A. Jossen, "Modeling and simulation of inhomogeneities in a 18650 nickel-rich, silicon-graphite lithium-ion cell during fast charging." *Journal of Power Sources*, **412**, 204 (2019).
4. O. Queisser, L. Cloos, F. Boehm, D. Oehler, and T. Wetzel, "Impact of the level of homogenization in 3D thermal simulation on the internal temperature distribution of Li-Ion battery cells." *Energy Technology*, **9**, 20009152194 (2021).
5. Z. Geng, J. Groot, and T. Thiringer, "A time- and cost-effective method for entropic coefficient determination of a large commercial battery cell." *IEEE Transactions on Transportation Electrification*, **6**, 257 (2020).
6. D. Bernardi, E. Pawlikowski, and J. Newman, "A general energy balance for battery systems." *J. Electrochem. Soc.*, **132**, 5 (1985).
7. G. Richardson and I. Korotkin, "Heat generation and a conservation law for chemical energy in li-ion batteries ." *Electrochimica Acta*, **392**, 138909 (2021).
8. D. Wycisk, G. K. Mertin, M. Oldenburger, and A. Latz, "Analysis of heat generation due to open-circuit voltage hysteresis in lithium-ion cells." *Journal of Energy Storage*, **61**, 106817 (2023).
9. F. Brosa Planella, "brosaplanella/tec-reduced-model: Published version." (2021) 10.5281/zenodo.4864437.
10. N. Damay, C. Forgez, M.-P. Bichat, and G. Friedrich, "A method for the fast estimation of a battery entropy-variation high-resolution curve—application on a commercial lifepo4/graphite cell." *Journal of Power Sources*, **332**, 149 (2016).
11. J. P. Schmidt, André Weber, and E. Ivers-Tiffée, "A novel and precise measuring method for the entropy of lithium-ion cells: ΔS via electrothermal impedance spectroscopy." *Electrochimica Acta*, **137**, 311 (2014).
12. A. Abbasalinejad, Münir M. Besli, J. W. Hammond, S. H. Chung, J. Christensen, and S. U. Kim, "Evaluation of the entropy of reaction using modified frequency-domain method and a physics-based thermoelectrochemical model of a lithium-ion battery." *Journal of Power Sources*, **508**, 230283 (2021).
13. A. Hales and J. Bulman, "A standardised potentiometric method for the effective parameterisation of reversible heating in a lithium-ion cell." *J. Electrochem. Soc.*, **171**, 050535 (2024).
14. Y. Hu, S.-Y. Choe, and T. R. Garrick, "Hybridized time-frequency method for the measurement of entropy coefficient of lithium-ion battery." *Electrochimica Acta*, **362**, 137124 (2020).
15. X.-F. Zhang, Y. Zhao, Y. Patel, T. Zhang, W.-M. Liu, M. Chen, G. J. Offer, and Y. Yan, "Potentiometric measurement of entropy change for lithium batteries." *Phys. Chem. Chem. Phys.*, **19**, 9833 (2017).
16. J. Xu, K. Xiong, T. Tang, Y. Chen, D. Hu, D. Hou, M. Yu, and J. Ding, "Precise determination of the continuous entropic coefficient profile of lithium-ion batteries using frequency-domain method." *Measurement*, **240**, 115578 (2025).
17. H. Akaike, "A new look at the statistical model identification." *IEEE Transactions on Automatic Control*, **19**, 716 (1974).
18. (Ljung), *System Identification* (Pearson, India) 2nd ed. (1998).
19. W. D. Widanage, A. Barai, G. H. Chouchelamane, K. Uddin, A. McGordon, J. Marco, and P. Jennings, "Design and use of multisine signals for li-ion battery equivalent circuit modelling. part 1: Signal design." *Journal of Power Sources*, **324**, 70 (2016).
20. Noël Hallemans, W. D. Widanage, X. Zhu, S. Moharana, M. Rashid, A. Hubin, and J. Lataire, "Operando electrochemical impedance spectroscopy and its application to commercial li-ion batteries." *Journal of Power Sources*, **547**, 232005 (2022).
21. M. Schroeder, "Synthesis of low-peak-factor signals and binary sequences with low autocorrelation (Corresp.)." *IEEE Trans. Inf. Theory*, **16**, 85 (1970).
22. R. Pintelon and J. Schoukens, *System Identification: A Frequency Domain Approach* (Wiley, New York) (2012).
23. J. S. Bendat and A. G. Piersol, *Engineering Applications of Correlation and Spectral Analysis* (Wiley, New York) (1993), https://books.google.de/books?id=DI1RAAAAMAAJ.
24. R. B. Blackman and J. W. Tukey, "The measurement of power spectra from the point of view of communications engineering—part i." *Bell Syst. Tech. J.*, **37**, 185 (1958).
25. G. M. Jenkins and D. G. Watts, *Spectral Analysis and Its Applications* (Holden-Day) (1969), Holden-Day series in time series analysis and digital signal processing https://books.google.de/books?id=1kBMAAAAMAAJ.
26. R. Pintelon, J. Schoukens, G. Vandersteen, and K. Barbé, "Estimation of nonparametric noise and FRF models for multivariable systems–Part I: Theory." *Mechanical Systems and Signal Processing*, **24**, 573 (2010).
27. W. D. Widanage, N. Omar, J. Schoukens, and J. Van Mierlo, "Estimating the frequency response of a system in the presence of an integrator." *Control Engineering Practice*, **35**, 1 (2015).
28. W. D. Widanage, A. Barai, G. H. Chouchelamane, K. Uddin, A. McGordon, J. Marco, and P. Jennings, "Design and use of multisine signals for Li-ion battery equivalent circuit modelling. Part 2: Model estimation." *Journal of Power Sources*, **324**, 61 (2016).
29. D. Werner, S. Paarmann, A. Wiebelt, and T. Wetzel, "Inhomogeneous temperature distribution affecting the cyclic aging of Li-ion cells. part i: Experimental investigation." *Batteries*, **6** (2020).
30. J. Huang, Z. Li, B. Y. Liaw, Z. Wang, S. Song, N. Wu, and J. Zhang, "Entropy coefficient of a blended electrode in a lithium-ion cell." *J. Electrochem. Soc.*, **162**, A2367 (2015).
31. M. E. Wojtala, A. A. Zülke, R. Burrell, M. Nagarathinam, G. Li, H. E. Hoster, D. A. Howey, and M. P. Mercer, "Entropy profiling for the diagnosis of NCA/Gr-SiOx Li-Ion battery health." *J. Electrochem. Soc.*, **169**, 100527 (2022).
32. M. P. Mercer, S. Finnigan, D. Kramer, D. Richards, and H. E. Hoster, "The influence of point defects on the entropy profiles of Lithium Ion Battery cathodes: A lattice-gas Monte Carlo study." *Electrochimica Acta*, **241**, 141 (2017).
33. M. P. Mercer, C. Peng, C. Soares, H. E. Hoster, and D. Kramer, "Voltage hysteresis during lithiation/delithiation of graphite associated with meta-stable carbon stackings." *Journal of Materials Chemistry A*, **9**, 492 (2021).
34. G. Assat, S. L. Glazier, C. Delacourt, and J.-M. Tarascon, "Probing the thermal effects of voltage hysteresis in anionic redox-based lithium-rich cathodes using isothermal calorimetry." *Nat. Energy*, **4**, 647 (2019).
35. M. Verbrugge, D. Baker, and X. Xiao, "Formulation for the treatment of multiple electrochemical reactions and associated speciation for the lithium-silicon electrode." *J. Electrochem. Soc.*, **163**, A262 (2016).
36. G. L. Plett, "Extended Kalman filtering for battery management systems of LiPB-based HEV battery packs Part 2. Modeling and identification." *Journal of Power Sources*, **134**, 262 (2004).
37. J. M. Foster, Y. Grudeva, I. Korotkin, E. J. F. Dickinson, G. J. Offer, and G. Richardson, "The newman model for phase-change electrodes: Physics-based hysteresis." *J. Electrochem. Soc.* (2025).